RSC Applied Interfaces

ROYAL SOCIETY OF CHEMISTRY

PAPER

View Article Online
View Journal | View Issue

Cite this: *RSC Appl. Interfaces*, 2026, 3, 431

Magnetic-field-induced enhanced electrochemical energy storage performance of nickel cobalt phosphide

Anuradha Yadav,[a] Erdenebayar Baasanjav,[b] Mihir Sahoo,[c] Kalpataru Pradhan,[d] Sang Mun Jeong, *[b] Manoj Kumar Singh *[ae] and Chandra Sekhar Rout *[bf]

Received 23rd September 2025,
Accepted 10th January 2026

DOI: 10.1039/d5lf00288e

rsc.li/RSCApplInter

In this work, NiCoP nanorods were synthesized using a combination of hydrothermal and phosphorization techniques. The carbon paper coated with NiCoP (NiCoP/CP) exhibited outstanding supercapacitive properties, achieving a specific capacitance of 264.528 F g^{-1} at a current density of 0.1 A g^{-1}, with 100% coulombic efficiency in both the absence and presence of a 400 G magnetic field. This enhancement was attributed to the alignment of magnetic dipoles caused by the Lorentz effect. The supercapacitor exhibited a peak specific energy density of 72.01 W h kg^{-1} and a maximum specific power density of 4219.92 W kg^{-1}, maintaining 57% of its initial capacitance after 5000 cycles under a 400 G magnetic field. Additionally, under the magnetic field, the reduced charge transfer resistance (R_{ct}) facilitated faster ion diffusion in the electrode, thereby enhancing its performance. Consequently, the bimetallic NiCoP/CP electrode prepared in this manner shows significant potential for energy storage and high-performance supercapacitor applications.

1. Introduction

The increasing environmental pollution, diminishing fossil fuels, and constantly increasing energy demands in storage devices have become urgent challenges.[1,2] Consequently, the demand for green, unpolluted, and sustainable energy sources and technologies has significantly increased, accelerating advancements in electrochemical energy conversion and storage systems.[3,4] The functioning of these energy storage systems is based on converting electrical energy derived from various sources into chemical energy.

The electrochemical capacitor, also known as a supercapacitor (SC), has garnered significant interest from the scientific community in recent years due to its high power density, long cycle stability, cost-effectiveness, rapid charging/discharging, and ease of reversibility.[5] SCs are the link between batteries, known for their greater energy storage capacity, and traditional capacitors, which deliver superior power outputs.[6,7] SCs are of two types: (1) electric double-layer capacitors (EDLCs), which store charge electrostatically, and (2) pseudocapacitors, depending on how they store charges, either by intercalation or a redox mechanism. In EDLCs, electrolyte ions are physically adsorbed onto the electrode surface, whereas in pseudocapacitors, charge storage occurs through redox reactions and ion intercalation within the electrode material.

Recently, a wide variety of SC electrode materials have been explored, including conducting polymers (*e.g.*, PANI, PPy, and PEDOT); metal hydroxides ($M(OH)_n$) such as $Ni(OH)_2$ and $Co(OH)_2$; metal oxides (RuO_2, MnO_2, Nb_2O_5, and SnO_2); metal chalcogenides ($FeSe_2$, MoS_2, and VS_2); and metal phosphides (CoP and FeP).[8,9] Among these, metal phosphides are regarded as promising SC electrode materials due to their metalloid nature, high electrical conductivity, narrow band gap, and excellent redox activity.[10] However, limited cyclic stability at higher mass loadings restricts the charge–discharge kinetics of transition metal phosphides (TMPs).[11] To address this challenge, various TMPs, including Co_2P, Ni_5P_4, MoP, Ni_xP, FeP, CoP, NiCoP, Mo_3P, and WP_2, have been synthesized using diverse methods to tailor their physical and chemical properties, such as conductivity, catalytic activity, and selectivity.[12,13] Bimetallic TMPs (*e.g.*, NiCoP, CuCoP,

[a] *Department of Physics and Astrophysics, School of Basic Sciences, Central University of Haryana, Jant-Pali, Mahendergarh-123031, India. E-mail: manojksingh@cuh.ac.in*
[b] *Department of Chemical Engineering, Chungbuk National University, Cheongju, Chungbuk 28644, Republic of Korea. E-mail: csrout@gmail.com*
[c] *Graz University of Technology, Graz, 8010, Austria. E-mail: mihir.sahoo@tugraz.at*
[d] *Theory Division, Saha Institute of Nuclear Physics, A CI of HBNI, Kolkata 700064, India. E-mail: kalpataru.pradhan@saha.ac.in*
[e] *Department of Applied Sciences and Humanities, School of Engineering and Technology (SOET), Central University of Haryana, Jant-Pali, Mahendergarh-123031, India*
[f] *Centre for Nano and Material Sciences, Jain (Deemed-to-be University), Jain Global Campus, Kanakapura Road, Bangalore – 562112, Karnataka, India. E-mail: r.chandrasekhar@jainuniversity.ac.in*

Zn–Ni–P, and NiFeP) exhibit lower adsorption energies and higher charge carrier densities than their single-metal counterparts, facilitating improved OH^- ion adsorption.[10] The presence of multiple oxidation states further enhances capacitance relative to monometallic TMPs.[14] Moreover, the strong synergistic interactions between nickel and cobalt promote redox reactions in bimetallic TMPs, resulting in enhanced electrical conductivity and improved structural stability.[15] Because Ni_2P offers a high specific capacity and Co_2P is known for its exceptional stability, Ni_xCo_yP is expected to integrate these advantages, delivering both high capacity and robust cycling performance, making it particularly attractive for SC applications.[16] NiCoP stores charges through faradaic reactions involving covalent Ni–P and Co–P bonds, while its metallic bonding provides free electrons for efficient charge transport. The electrochemical performance of NiCoP is strongly influenced by its morphology, including 3D hollow structures, nanoparticles, and 1D hollow architectures.[17–19] Nevertheless, NiCoP-based SCs continue to face challenges such as poor cyclic stability, limited rate capability, and irreversible volume changes during repeated charge–discharge processes.[20]

Huang *et al.* fabricated NiCoP directly on a nickel foam, where the porous NiCoP electrode was activated through 50 cycles of cyclic voltammetry. After activation, cracks developed on the uneven microspheres, accompanied by the formation of numerous small mesopores. Efficient ion diffusion and charge transport are critical for enhancing the SC's performance, and electrode architectures with abundant active sites promote unobstructed electrolyte ion migration. Li *et al.* developed porous NiCoP nanocubes with a large architectural surface area. The $Ni_{0.5}Co_{0.5}(OH)_2$ intermediate was first obtained by modifying a Cu_2O template with $S_2O_3^{2-}$, which was subsequently phosphorized using PH_3 to form a hollow NiCoP structure.[21] Similarly, He *et al.* synthesized NiCoP supported on carbon cloth (NiCoP/CC), which exhibited a higher capacity than Ni_2P/CC due to its staggered nanosheet morphology (~20 nm thick) and hierarchical three-dimensional nano-microstructure.[22]

The motion of charge carriers in coupled electric and magnetic fields is strongly dependent on the relative orientation of the two fields. When a magnetic field exerts a Lorentz force on moving ions, it influences the key electrochemical parameters of SCs, including capacitance, diffusion coefficient, ionic mobility, and the electrical conductivity of the electrode material. The SC's performance under a magnetic field can be enhanced through two main strategies: (1) the incorporation of magnetic nanomaterials and (2) the polarization and reconstruction of the charge density within magnetic materials.[23] Magnetic fields can accelerate electrochemical reaction kinetics by modifying the electrode material and shortening the diffusion pathways of electrolyte ions. In addition, they guide ion arrangement and promote chemical reactions by increasing the chemical potential gradient and magnetic free energy, thereby improving microstructural stability and optimizing the elemental composition.[24,25] The magnetic field effect also enhances electrolyte convection, activates the electrode surface by reducing the thickness of the Nernst diffusion layer, and lowers the interfacial resistance between the electrode and electrolyte. Moreover, the Lorentz force induced by the magnetic field facilitates deeper ion insertion and intercalation, leading to enhanced capacitance.[26] Although several electrodeposition strategies have been developed to increase mass loading, they are often constrained by limited exposure of active sites. For example, the loading of NiCo layered double hydroxide (NiCo-LDH) nanosheets was improved by increasing the precursor concentration or by constructing heterostructured electrodes.[27] In this regard, Li *et al.* electrodeposited NiCo-LDH onto $Ti_3C_2T_x$-coated carbon cloth under an optimized parallel magnetic field of 3 T, producing a nest-like architecture with an areal capacity of 3.12 C cm^{-2} at 1 mA cm^{-2}.[28] Furthermore, Li *et al.* introduced Fe into NiCo-LDH assembled on a nickel foam, where spin interactions regulated redox reactions by redistributing surface electrons around the Ni and Co active sites.[29]

In this study, NiCoP nanorods were synthesized *via* a hydrothermal method, followed by phosphorization, and subsequently deposited onto a carbon paper substrate. The supercapacitor's performance was assessed in a 1 M KOH solution, both in the presence and absence of a magnetic field. Introducing a magnetic field notably increased the supercapacitor's specific capacitance from 102.085 F g^{-1} to 264.528 F g^{-1} at a current density of 0.1 A g^{-1} under the maximum magnetic field strength of 400 G. The material achieved a peak energy density (E_{max} = 72.01 W h kg^{-1}) and a peak power density (P_{max} = 4219.92 W kg^{-1}), maintaining 100% coulombic efficiency at 400 G. Furthermore, the Lorentz force acting on the ions aligned the magnetic dipoles in the direction of the magnetic field, reducing charge transfer resistance. The supercapacitive properties of NiCoP were also explored using density functional theory (DFT). Spin–orbit interactions, along with nonlinear magnetic spin phenomena across different configurations, were utilized to evaluate the quantum capacitance.

2. Experimental

2.1 Material synthesis

First, $Co(NO_3)_2{\cdot}6H_2O$ (1 mmol), $Ni(NO_3)_2{\cdot}6H_2O$ (0.5 mmol), $CO(NH_2)_2$ (3 mmol), and NH_4F (1 mmol) were stirred in distilled water at RT for 20 minutes. The mixture was then transferred to a 50 mL autoclave and subjected to a reaction at 120 °C for 6 hours. The resulting material was washed with ethanol and distilled water, followed by overnight drying in an oven. Subsequently, the NiCo-LDH powder was phosphorized with sodium hypophosphite in a ratio of 1 : 10 in a nitrogen atmosphere at 350 °C with a ramp rate of 2 °C min^{-1} for 2 hours (Fig. 1). Finally, the obtained sample was named as NiCoP.[30]

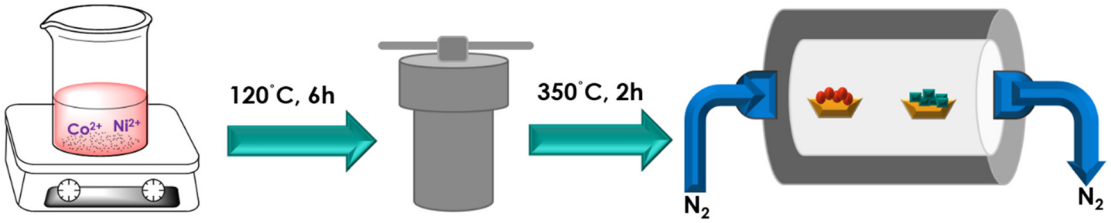

Fig. 1 Schematic of the NiCoP synthesis.

2.2 Characterizations

X-ray diffraction (XRD) with CuK_α radiation (wavelength = ~0.154 nm) was used to evaluate the material's crystal structure within the 2θ range from 10° to 80° at a scan rate of 1° min^{-1} (Rigaku Company, Japan). The surface morphology was examined using field-emission scanning electron microscopy (FE-SEM; Carl Zeiss, Ultra Plus, LEO-1530) and transmission electron microscopy (TEM; JEM-2100F, UHR, JEOL, KBSI). X-ray photoelectron spectroscopy (XPS; PHI Quantera-II, AlK_α radiation, Ulvac-PHI) was employed to analyze the oxidation states. The magnetic properties were assessed using a Microsense model ADE EV9 vibrating sample magnetometer. The electrochemical performance of the

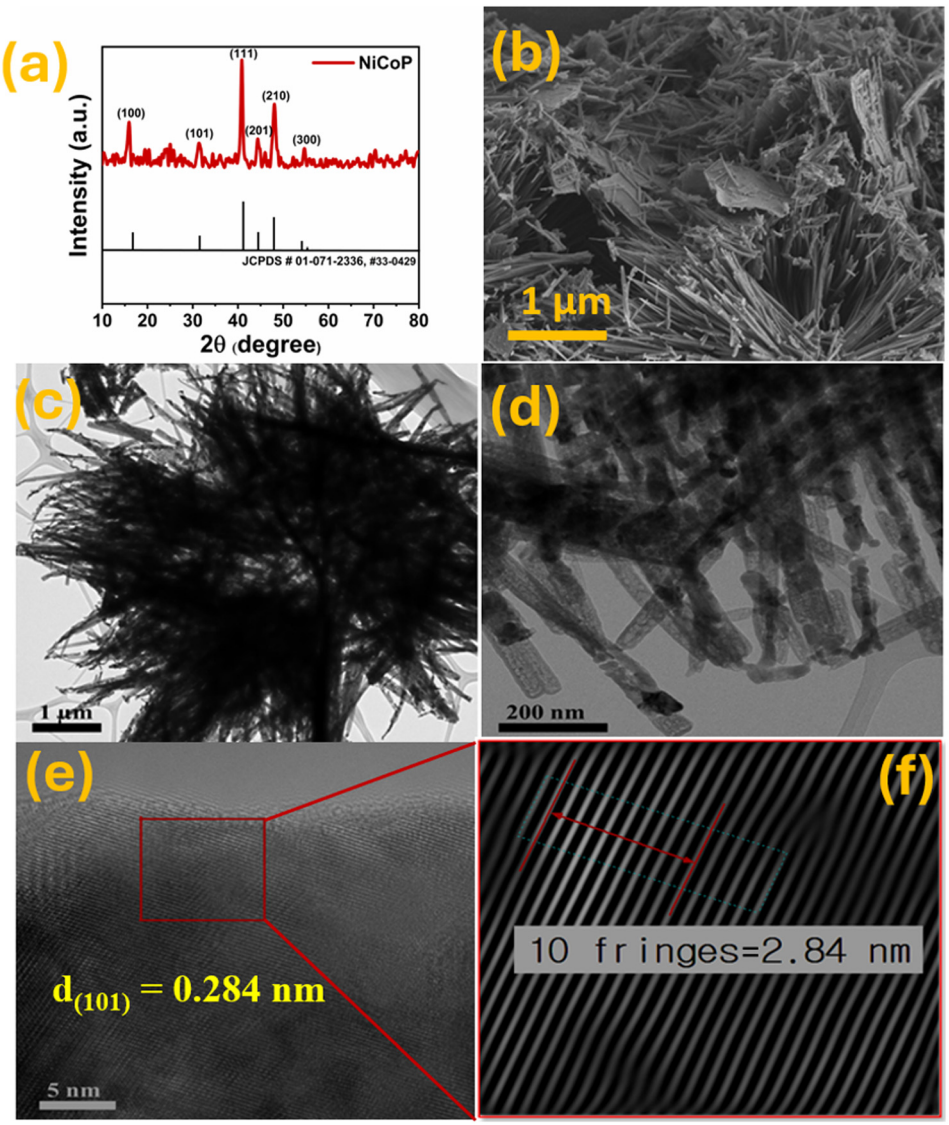

Fig. 2 (a) XRD pattern; (b) FESEM image; (c–f) TEM images; and (e) and (f) lattice fringes for the (101) plane of NiCoP.

supercapacitor was evaluated using the CorrTest electrochemical workstation (CS350) and CS Studio software to determine the required parameters.

2.3 Electrochemical analysis

The electrochemical characteristics were examined in an alkaline medium using the CorrTest electrochemical workstation. The three-electrode setup was positioned between the magnet coils, with the working electrode oriented along the magnetic field direction. A Hg/HgO electrode was used as the reference electrode, while a platinum coil functioned as the counter electrode.

The charge storage performance of the sample in a three-electrode configuration was calculated using cyclic voltammetry (CV), galvanostatic charge/discharge (GCD) analysis, and electrochemical impedance spectroscopy (EIS). The following equations were used to calculate the specific capacitance (C_s, F g^{-1}), energy density (E_s, W h kg^{-1}), and power density (P_s, W kg^{-1}):

$$C_s\,(\mathrm{GCD}) = \frac{I \times \Delta t}{m \times \Delta V} \quad (1)$$

$$E_s = \frac{1}{2} \times C_s \times (\Delta V)^2 \times \frac{1000}{3600} \quad (2)$$

$$P_s = \left(\frac{E_s}{\Delta t}\right) \times 3600 \quad (3)$$

where Δt is the discharge time (s), ΔV is the potential window (V), m is the active mass of the electrode (mg), and I is the current (mA).

3. Results and discussion

The XRD was performed within the 2θ range from 10° to 80°. The diffraction peaks at 2θ angles of 17.54°, 32.02°, 40.86°, 44.4°, 47.8°, and 54.4° correspond to the planes (100), (101), (111), (201), (210), and (300) of NiCoP, respectively, thereby confirming consistency with JCPDS no. 01-071-2336 and 33-0429 (Fig. 2(a)). The surface morphology of NiCoP was examined using FESEM at different magnifications, as shown in Fig. 2(b) and S2(a and b). The sample exhibits a nanorod structure. The highest peak intensity of the (111) plane in the XRD pattern, occurring at an angle of 40.86°, indicates the preferential orientation of the nanorods. The morphology of NiCoP was analyzed using transmission electron microscopy (TEM).

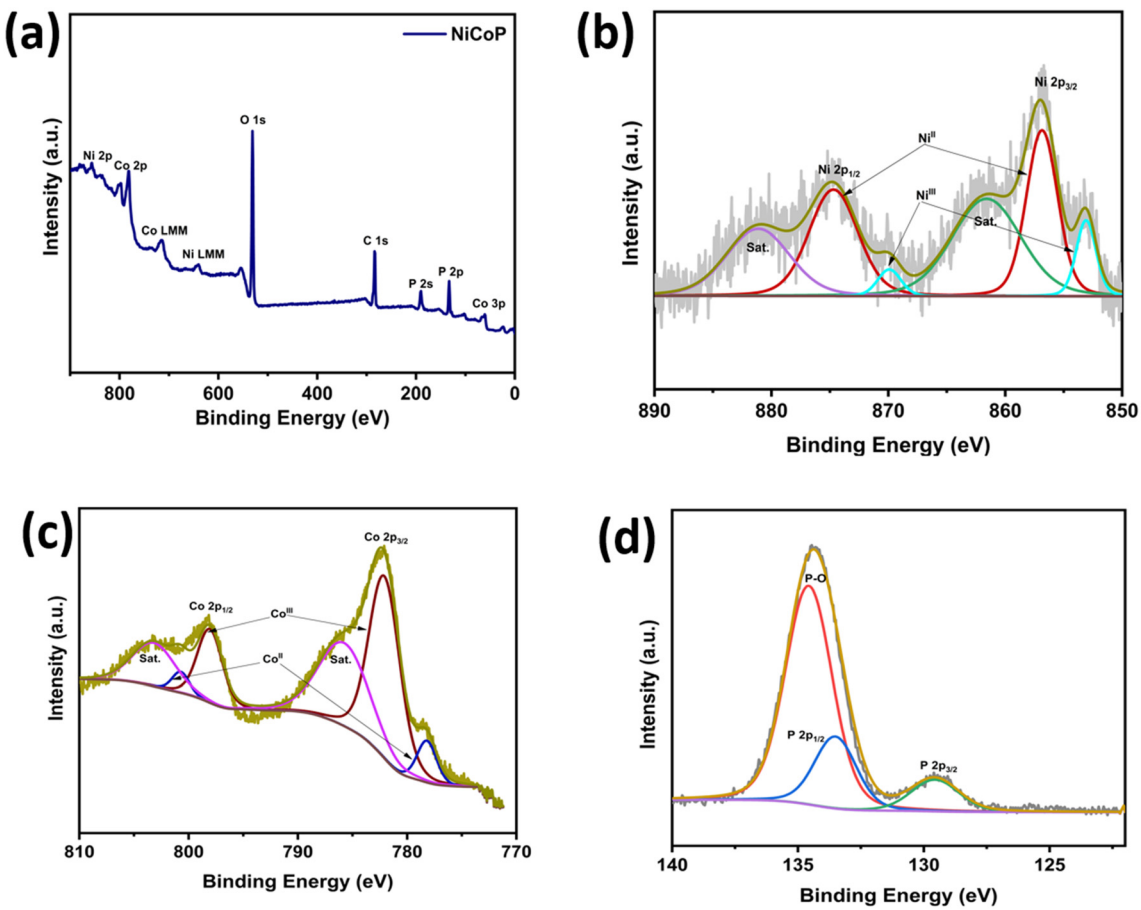

Fig. 3 XPS spectra of (a) NiCoP, (b) Ni 2p, (c) Co 2p, and (d) P 2p.

Fig. 2(c and d) presents the TEM images of NiCoP nanorods at different magnifications, while Fig. 2(e and f) displays the lattice fringes with a *d*-spacing of 0.284 nm for the (101) plane.

XPS analysis was conducted to determine the surface chemical composition and the valence states of the elements. Apart from Ni, C, and P, no other impurity peaks are detected in the spectrum during sample preparation (Fig. 3(a)). Fig. 3(b) shows the XPS spectrum of Ni 2p, in which the two peaks at binding energies of 853.5 eV and 870.5 eV correspond to Ni^{3+} $2p_{3/2}$ and Ni^{3+} $2p_{1/2}$, respectively, confirming the presence of the +3 oxidation state. Additionally, the peaks at 856.3 eV and 874 eV correspond to Ni^{2+} $2p_{3/2}$ and Ni^{2+} $2p_{1/2}$, confirming the presence of the +2 oxidation state, along with the satellite peaks at 861.3 eV and 879.4 eV. The Co 2p spectrum exhibits satellite peaks at 784.8 ($2p_{3/2}$) and 802.7 eV ($2p_{1/2}$), along with binding energies of 778.67 eV and 781.02 eV for Co^{3+} $2p_{3/2}$ and Co^{2+} $2p_{3/2}$ and 793.62 eV and 797.37 eV for Co^{3+} $2p_{1/2}$ and Co^{3+} $2p_{1/2}$, respectively, confirming the presence of both +2 and +3 oxidation states (Fig. 3(c)). The peaks at 130.4 eV and 133.6 eV confirm the presence of metal phosphide and oxidized phosphorus (PO_4^{3-} and P_2O_5), respectively [Fig. 3(d)].[30]

3.1 Electrochemical investigations

The supercapacitor electrode was fabricated using carbon paper as the substrate. A slurry was obtained by combining the active material, carbon black, and PVDF in a 8 : 1 : 1 ratio and then continuously grinding it in *N*-methyl pyrrolidone (NMP) to obtain a homogeneous mixture. This slurry was then layered onto the substrate. A 1 cm × 1 cm piece of carbon paper was deposited with 2 mg of the active substance over an area of 0.5 cm × 1 cm. The layered substrate was oven-dried overnight at 60 °C. Once dried, it was used as the working electrode.

Fig. 4(a) presents a schematic illustration of the three-electrode setup in an external magnetic field. Without a magnetic field, charged particles experience only the electrostatic force due to the potential, meaning that only $q\vec{E}$ contributes to the Lorentz force. However, when a magnetic field is applied, $q(\vec{E} \times \vec{B})$ acts on the charged particles, driving the ionic species to intercalate into the electrode material.[31,32] The magnetic field affects the thickness of the Nernst diffusion layer, facilitating the movement of electrolyte ions into the electrode material. A magnetic gradient force also arises from the non-uniform distribution of charged species. The magnetic field promotes redox reactions and establishes pathways for electron and ion transport by diminishing the Nernst layer thickness, thereby enhancing the electrode's capacity for charge storage. The spin degeneracy is an additional factor that enhances the ion convection, lowers the inherent resistance, and boosts the charge retention capacity of the electrode material.[33] However, at higher magnetic field strengths, the capacitance diminishes as a result of strong coulombic interactions between positively and negatively charged electrolyte ions.[34]

In an alkaline medium, OH^- ions polarize water molecules by forming hydrogen bonds and experience the Lorentz force when exposed to a magnetic field.[34] In an alkaline medium, NiCoP follows the following mechanism:[35]

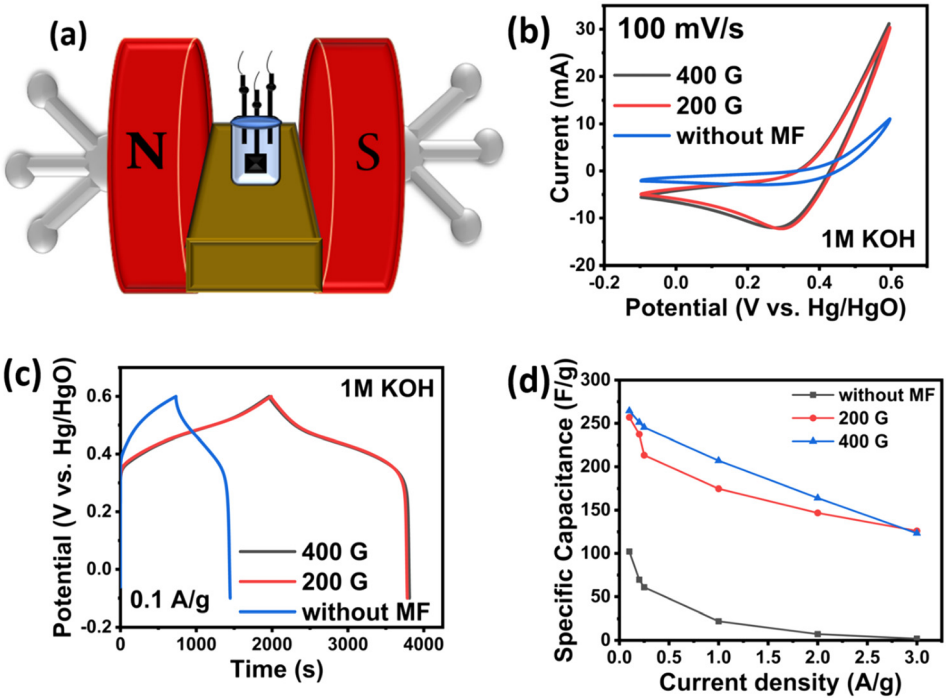

Fig. 4 (a) Schematic of the magnetic electrochemical setup; (b) CV curves at 100 mV s^{-1}; (c) GCD curves at 0.1 A g^{-1} of NiCoP; and (d) specific capacitances at 0.1–3 A g^{-1} for NiCoP.

$$NiCoP + OH^- \leftrightarrow NiCoPOH + e^- \quad (4)$$

$$NiCoPOH + OH^- \leftrightarrow 2NiCoPO + H_2O + e^- \quad (5)$$

CV, GCD, and EIS measurements were performed using a three-electrode setup within the potential window from −0.1 V to 0.6 V. The CV and GCD curves' shapes (Fig. 4(b and c)) validated the battery-type behavior of the sample. The CV curve displayed a cathodic peak, which shifted toward a higher potential as the scan rate was reduced, without altering the overall shape of the curve, suggesting a polarization phenomenon.[36,37] As the magnetic field increased, the area under the CV curve increased, suggesting that the magnetic field plays a role in enhancing charge storage, reducing internal resistance, and improving the electrode's conductivity.[38] Fig. S4(a–c) shows the CV curves at different scan rates from 10 to 100 mV s^{-1}, and Fig. S4(d–f) shows the GCD curves at current densities from 0.1 A g^{-1} to 3 A g^{-1} in the absence and presence of magnetic fields.

The specific capacitance at different current densities is shown in Fig. 4(d). After the application of a magnetic field, NiCoP displayed specific capacitances of 256.937 F g^{-1} at 200 G and 264.528 F g^{-1} at 400 G, in contrast to 102.085 F g^{-1} without a magnetic field. This corresponded to an increase in the specific capacitance of 151.7% at 200 G and 159.1% at 400 G compared to that without a magnetic field. Beyond a certain magnetic field strength, the magnetic dipoles were aligned with the field, diminishing the impact of the Lorentz force. This saturation of magnetic dipoles consequently resulted in a decrease in the specific capacitance.

Eqn (2) and (3) were applied to calculate the energy and power densities, respectively. The sample demonstrated E_{max} of 72.01 W h kg^{-1} and 27.790 W h kg^{-1} and P_{max} of 4219.92 W kg^{-1} and 4201.2 W kg^{-1} with and without magnetic exposure, respectively. The Nyquist plot was obtained to evaluate the supercapacitive behavior by portraying the link between the real and imaginary impedance elements. The graph exhibited a semicircular segment at higher frequencies and a slanted line at lower frequencies, spanning from 1 MHz to 1 mHz, with a 10 mV bias alternating voltage in both the absence and presence of the magnetic field. This plot provided a clear understanding of the reaction mechanism involved and the different resistances presented by various electrolytes. The corresponding equivalent fitted circuit is displayed in the inset of Fig. 5(a). The *x*-intercept signifies the solution resistance (R_s), whereas the semicircle represents the charge transfer resistance (R_{ct}), reflecting the resistance that electrolyte ions encounter during diffusion. The R_{ct} decreased from 8.727 Ω without a magnetic field to 2.249 Ω at 400 G, indicating an enhancement in the electrode's conductivity. The Warburg resistance (W_s) represented the diffusion of electrolyte ions into the electrode material.[39] The deviation of the straight line toward the *y*-axis indicated enhanced ion diffusion within the electrode material under the influence of a magnetic field.[40]

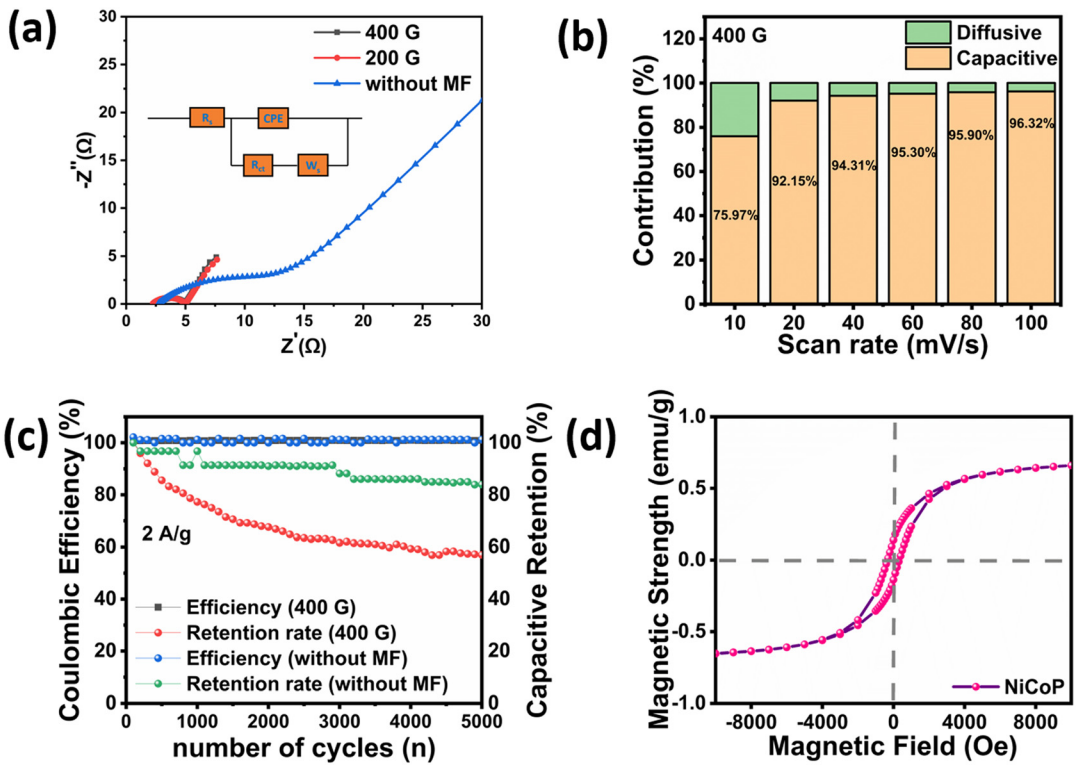

Fig. 5 (a) Nyquist plot; (b) capacitive and diffusive contributions; (c) cyclic stability at 2 A g^{-1}; and (d) *M–H* curve of NiCoP.

The total charge is stored on the electrode surface by two processes: the faradaic process or the non-faradaic process. The faradaic process involves either redox reactions or an intercalation process inside the electrode. Conversely, the charge is electrostatically stored on the electrode surface *via* the capacitive process. Fig. 5(b) depicts the capacitive and diffusive contributions at scan rates from 10 to 100 mV s^{-1} under a 400 G magnetic field. At a high scan rate of 100 mV s^{-1}, the electrochemical response was largely capacitive, contributing 96.32%, while the diffusive contribution was limited to 3.68%. As the scan rate decreased to 10 mV s^{-1}, the diffusive contribution increased to 24.03%, accompanied by a reduction in the capacitive contribution to 75.97%. This behavior is attributed to the magnetic field effect, whereby electrolyte ions subjected to the Lorentz force gain sufficient time to diffuse into the electrode matrix, thereby facilitating redox reactions or intercalation processes.

The overall current response results from the combined capacitive and diffusive contributions (eqn (6) and (7)).

$$i(V) = I_{cap} + I_{diff}, \quad (6)$$

$$i(V) = k_1 v + k_2 v^{1/2}, \quad (7)$$

where $k_1 v$ is the capacitive contribution and $k_2 v^{1/2}$ is the diffusive current contribution. The total current and capacitive current response at a 40 mV s^{-1} scan rate are shown in the CV plot (Fig. S5).[41,42]

The coulombic efficiency and retention rate of NiCoP were also tested to ensure its cycle stability, a crucial factor for supercapacitor applications. The supercapacitor demonstrated prolonged cyclic stability at a current density of 2 A g^{-1}. The electrode maintained a stable coulombic efficiency of 100% under both magnetic and nonmagnetic conditions, with capacitive retentions of 57% at 400 G and 84.9% without a magnetic field after 5000 cycles (Fig. 5(c)). Even though the coulombic efficiency remained close to 100%, the capacitance retention decreased noticeably to 57% after 5000 cycles at 400 G. This discrepancy arises because coulombic efficiency reflects the reversibility of the charge–discharge process during individual cycles, whereas capacitance retention indicates the long-term structural and electrochemical stability of the electrode. The observed capacitance fading is likely attributable to gradual electrode degradation, such as partial loss of the active material or increased internal resistance, which has little effect on the charge balance during each cycle. The XRD and SEM analyses after stability tests in the absence and presence of a magnetic field are shown in Fig. S1 and S3, respectively.

Fig. 5(d) illustrates the *M–H* hysteresis curves of NiCoP at room temperature. The saturation magnetization and magnetic field, measured using a vibrating sample magnetometer (VSM), were 0.71 emu g^{-1} and 7000 Oe (1 Oe = 79.59 A m^{-1}), respectively. Magnetization refers to the extent to which magnetic dipoles uniformly point in the direction of the magnetic field within a magnetic material. The narrow hysteresis loop displayed the characteristic features of a soft ferromagnetic material, with low coercivity and low retentivity, enabling easy magnetization and demagnetization.[43] The comparative study of NiCoP nanorods with a previous reported study is shown in Table 1.

3.2 DFT study

First-principles density functional theory (DFT) calculations were performed using the Vienna *ab initio* simulation package (VASP) to investigate the geometrical and electronic structural properties of the NiCoP surface.[44,45] For the exchange–correlation functional, the Perdew–Burke–Ernzerhof (PBE) form of the generalized gradient approximation (GGA) was adopted. At the same time, the pseudopotentials were described using the projector augmented wave (PAW) approach. A kinetic energy cutoff of 500 eV was chosen to expand the plane-wave basis set. Within the Monkhorst–Pack scheme, 4 × 4 × 1 and 7 × 7 × 1 *k*-point grids were used to sample the Brillouin zone for self-consistent field (SCF) and density of states (DOS) calculations, respectively.[46] To preserve the slab geometry and prevent interactions between periodic images, a vacuum layer of 20 Å was introduced along the *Z*-direction of the supercell. All atoms were fully relaxed until the Hellmann–Feynman forces on each atom were less than 0.01 eV $Å^{-1}$ and the total energy difference between two consecutive electronic steps was less than 10^{-5} eV. Non-collinear magnetic (NCL) calculations, including spin–orbit coupling (SOC), were performed to study the variation in the system's supercapacitance under an external magnetic field.

The quantum capacitance (C_Q) is defined as follows:

$$C_Q = \frac{d\sigma}{d\phi} \quad (8)$$

where σ and ϕ represent the surface charge density and local electrostatic potential of the NiCoP surface, respectively. As the electrochemical potential (μF) of a system shifts linearly with the external electrostatic potential (ϕ), the corresponding excess surface charge density (ΔQ) can be calculated as follows:[47]

$$\Delta Q = -e \int_{-\infty}^{+\infty} D(E)[f(E) - f(E-\phi)]dE \quad (9)$$

In the above expression, $D(E)$, $f(E)$, and e denote the density of states (DOS), Fermi–Dirac distribution, and elementary charge, respectively. Energy relative to the Fermi level is given by E. Thus, C_Q can be reformulated as follows:

$$\Delta C_Q = e^2 \int_{-\infty}^{+\infty} D(E)\, F_T(E-\phi)dE \quad (10)$$

Here, $F_T(E)$ denotes the thermal broadening function, which explains the temperature dependency of electron occupation and can be expressed in terms of the Boltzmann constant (k_B) and temperature (T = 300 K for this study), as follows:

$$F_T(E) = \frac{1}{4k_B T} \operatorname{sech}^2\left(\frac{E}{2k_B T}\right) \quad (11)$$

As illustrated in Fig. 6(a), the NiCoP(111) surface was constructed using a 1 × 1 supercell in the *ab* plane, comprising three atomic layers with a total thickness of approximately 6.1 Å along the *c* direction. Each atomic layer contained three Co, three Ni, and three P atoms arranged to preserve stoichiometry and surface symmetry. This model was considered to investigate the supercapacitance properties. According to the initial collinear magnetic calculations, the system exhibited ferromagnetic (FM) ordering with a total magnetic moment of around $4.54\mu_B$, primarily contributed ($\sim 1.2\mu_B$ each) by the Co atoms of the top layer. In contrast, Ni atoms and the rest of the Co atoms contributed minimally to the total magnetic moment of the system.

To further explore the influence of an external magnetic field on the supercapacitance, non-collinear magnetic calculations, including the spin–orbit coupling (SOC) effect, were performed. The effect of the magnetic field was modelled indirectly by varying the spin alignment direction among the surface atoms. In this model, the fully collinear FM configuration, with all spins aligned along the same

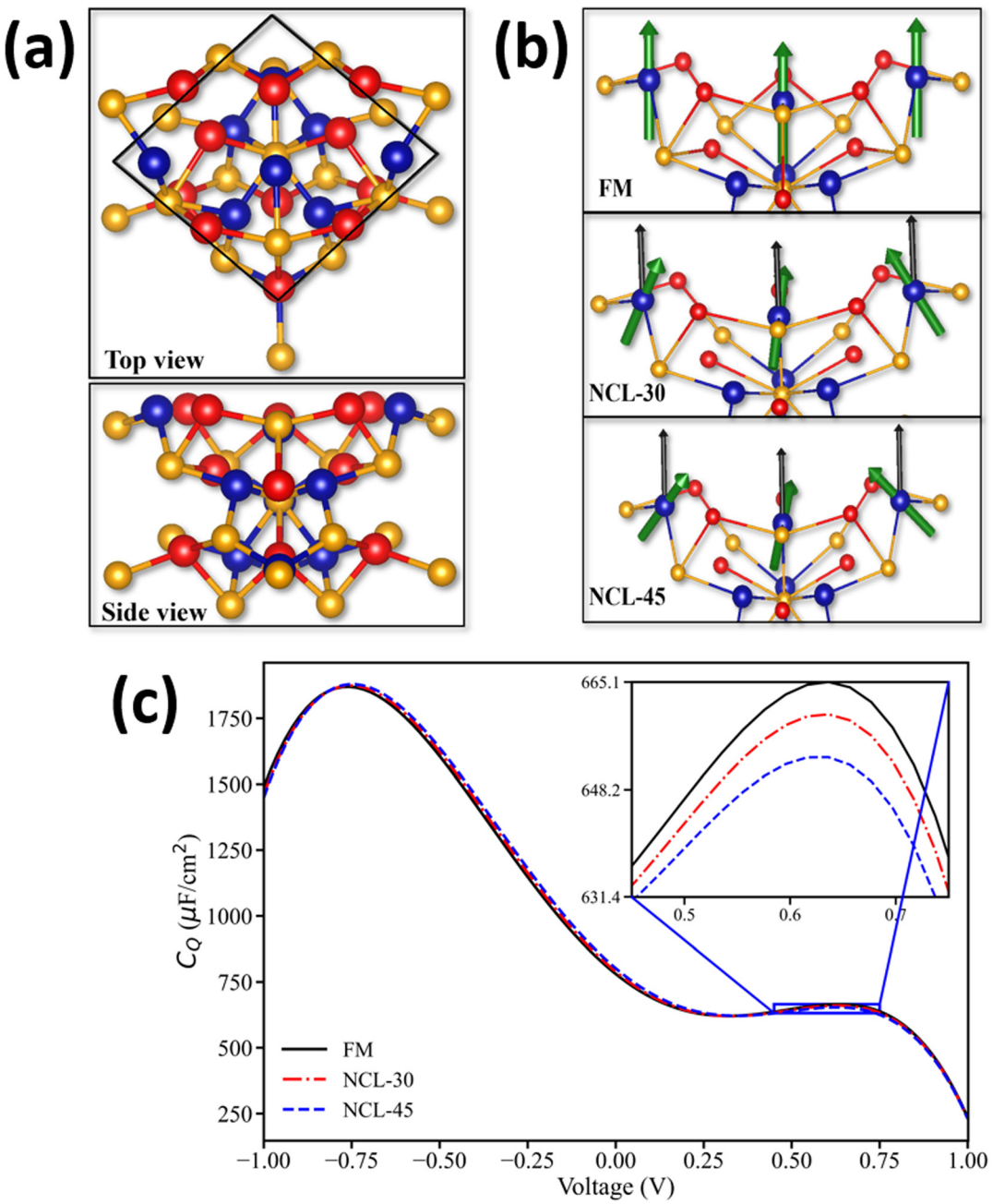

Fig. 6 (a) Top and side views of the NiCoP(111) surface. (b) Schematic of three different spin configurations, where green arrows indicate spin orientations and black arrows denote the *z*-axis direction. (c) Quantum capacitance (QC), C_Q, as a function of the voltage for the three configurations (Co, Ni, and P atoms are depicted in blue, red, and orange spheres, respectively). The inset shows a magnified view of the C_Q–V curve in the region 0.45–0.75 V.

Table 1 Comparative study of NiCoP nanorods with the previous reports

Electrode material	Specific capacitance (F g^{-1})	Electrolyte	Capacitive retention	References
NiO	209 F g^{-1} at 0.5 A g^{-1}	2 M KOH	98% (1000 cycles)	50
mr10-500-C/CoSi/CoO	246.6 F g^{-1} at 0.5 A g^{-1}	1 M KOH	88.06% (1000 cycles)	51
CoO_x/C	189 F g^{-1} at 1 A g^{-1}	6 M KOH	69% at 10 A g^{-1}	52
$Ni_{12}P_5$-rGO	192 F g^{-1} at 1 A g^{-1}	3 M KOH	89% (5000 cycles)	53
$FeCo_2O_4$ (30 G)	111 F g^{-1} at 0.25 A g^{-1}	2 M KOH	93% (2000 cycles)	54
α-Fe_2O_3-PR2 (200 G)	82 F g^{-1} at 1 A g^{-1}	1 M KOH	98% (1000 cycles)	55
NiCoP (400 G)	264.528 F g^{-1}	1 M KOH	57% (5000 cycles)	This work

direction, represented the state induced by a strong external magnetic field. Particular focus was given to the collinearity *vs.* non-collinearity of the three cobalt atoms in the top layer. Initially, a configuration referred to as the "FM surface", in which spins of all three surface Co atoms were kept aligned parallel to the *c*-axis of the supercell, yielding a total magnetic moment of 4.54μ_B, was considered.

In addition to the collinear FM configuration, two non-collinear magnetic configurations were modeled by tilting the spins of the Co atoms at specific angles. In the first case, referred to as NCL-30, the spins of the three Co atoms were aligned at a polar angle of 30° with respect to the *z*-axis and azimuthal angles (measured in the *xy*-plane from the *x*-axis) of 0°, 120°, and 250°, respectively. This configuration reduced the net magnetic moment along the *z*-direction. A similar configuration, denoted as NCL-45, was also considered, where the spins were tilted at a polar angle of 45°. The spin orientations of these three configurations are schematically shown in Fig. 6(b). The NCL-30 and NCL-45 configurations exhibited total energies that were 35.87 meV and 67.34 meV higher, respectively, than that of the collinear FM system, with corresponding reductions in the net magnetic moment along the *z*-direction to 3.98μ_B and 3.21μ_B. The net magnetic moment along the *z*-direction decreased as we moved from FM to NCL-30 to NCL-45. These NCL configurations with a reduced net magnetic moment could be related to experimental setups with weaker magnetic fields. Therefore, overall, the collinear FM configuration serves as a benchmark state in the presence of a magnetic field, while the NCL configurations serve as metastable states in our calculations, and the reduced magnetic moments typically mimic the systems that deviate from this ideal parallel alignment configuration state in the absence of a magnetic field or in the presence of comparatively smaller magnetic fields. This transition from non-collinear to collinear configurations can alter the density of states (DOS) near the Fermi level, thereby influencing the quantum capacitance (QC) of the system.[48,49] By correlating the spin-canting angles with the resulting electronic structure, our aim was to replicate the experimental trends where the FM ordered configuration at positive voltages led to an increase in the QC.

The quantum capacitance of these three systems within the voltage range from −1.0 to +1.0 V is shown in Fig. 6(c). As shown in the figure, at negative voltages (and very low positive voltages), the QC values of the NCL-30 and NCL-45 systems were slightly higher than those of the FM configuration. At 0 V, the QC values were 780 μF cm^{-2}, 789 μF cm^{-2}, and 801 μF cm^{-2} for the FM, NCL-30, and NCL-45 configurations, respectively. However, as the voltage increased, this trend reversed, and at 0.34 V, the QC value of the FM system surpassed those of the other two configurations. At 0.64 V, the QC values were 665 μF cm^{-2}, 660 μF cm^{-2}, and 653 μF cm^{-2} for the FM, NCL-30, and NCL-45 configurations, respectively (inset, Fig. 6(c)). These results are consistent with our experimental observations, where the application of a magnetic field was found to enhance the supercapacitance at positive voltages.

4. Conclusion

In summary, NiCo-LDH was synthesized *via* a hydrothermal route and subsequently converted into NiCoP nanorods through phosphorization. Electrochemical investigations revealed the superior capacitive performance of NiCoP in a 1 M KOH electrolyte under a magnetic field. The applied magnetic field enhanced the electrochemical behavior by increasing the availability of functional surface sites and shortening the diffusion pathways of OH^- ions. Under a magnetic field of 400 G, the material exhibited excellent charge-storage capability, delivering a high specific capacitance of 264.528 F g^{-1}, along with a specific energy of 72.01 W h kg^{-1} and a specific power of 4.21 kW kg^{-1}.

According to theoretical modelling, the ferromagnetic (FM) system showed a higher quantum capacitance (QC) at a positive potential of 0.64 V compared to NCL-30 and NCL-45, whereas NCL-30 and NCL-45 demonstrated superior QC in lower positive and negative voltage ranges, respectively. The ferromagnetically aligned Co atoms in the FM system, NCL-30, and NCL-45 yielded total magnetic moments of 4.54μ_B, 3.98μ_B, and 3.21μ_B, respectively. Overall, the engineered structure provides a versatile platform suitable for water splitting, batteries, wearable devices, and a wide range of next-generation energy storage applications (Table 1).

Author contributions

Anuradha Yadav: formal analysis, investigation, methodology, writing – original draft. Erdenebayar Baasanjav: investigation, methodology. Mihir Sahoo: investigation, dft analysis, writing. Kalpataru Pradhan: investigation, dft analysis, supervision. Sang Mun Jeong: funding acquisition,

supervision, writing – review & editing. Chandra Sekhar Rout: conceptualization, funding acquisition, supervision, writing – review & editing. Manoj Kumar Singh: supervision, writing – review & editing.

Conflicts of interest

The authors have no conflicts to disclose.

Data availability

The corresponding author can provide the data supporting the study's conclusions upon reasonable request.

Supplementary information (SI) is available. See DOI: https://doi.org/10.1039/d5lf00288e.

Acknowledgements

The authors extend their appreciation for the financial assistance provided by the Joint CSIR-UGC (ref. no. 211610041524 (24/03/2022)), the ANRF Core Research Grant (Grant No. CRG/2022/000897), and Jain University (JU/MRP/CNMS/118/2025). C. S. R. acknowledges support from the National Research Foundation of Korea under the Brain Pool program, funded by the Ministry of Science and ICT, South Korea (grant no. RS-2023-00222186). The work is further supported by the National Research Foundation of Korea (NRF) funded by the Ministry of Science and ICT (Grant No. 2024-00345983) and Regional Innovation System & Education (RISE) program through the Chungbuk Regional Innovation System & Education Center, funded by the Ministry of Education (MOE) and the Chungcheongbuk-do, Republic of Korea (2025-RISE-11-014-03).

References

1 J. Liu, X. Deng, S. Zhu, N. Zhao, J. Sha, L. Ma and F. He, *Electrochim. Acta*, 2021, **368**, 137528.
2 S. Kavian, S. Hajati and M. Moradi, *J. Mater. Sci.: Mater. Electron.*, 2021, **32**, 13117–13128.
3 G. Wang, L. Zhang and J. Zhang, *Chem. Soc. Rev.*, 2012, **41**, 797–828.
4 C. P. Grey and J. M. Tarascon, *Nat. Mater.*, 2016, **16**, 45–56.
5 T. Zhao, C. Liu, F. Yi, X. Liu, A. Gao, D. Shu and J. Ling, *Appl. Surf. Sci.*, 2021, **569**, 151098.
6 M. Pershaanaa, S. Bashir, S. Ramesh and K. Ramesh, *J. Energy Storage*, 2022, **50**, 104599.
7 F. Naseri, S. Karimi, E. Farjah and E. Schaltz, *Renewable Sustainable Energy Rev.*, 2022, **155**, 111913.
8 C. Guo, Y. Zhang, M. Yin, J. Shi, W. Zhang, X. Wang, Y. Wu, J. Ma, D. Yuan and C. Jia, *J. Power Sources*, 2021, **485**, 229315.
9 C. Zhang, Z. Peng, Y. Chen, H. Chen, B. Zhang, H. Cheng, J. Wang and M. Deng, *Electrochim. Acta*, 2020, **347**, 136246.
10 L. Wan, Y. Wang, Y. Zhang, C. Du, J. Chen, M. Xie, Z. Tian and W. Zhang, *J. Power Sources*, 2021, **506**, 230096.
11 X. Lei, S. Ge, T. Y. Yang, Y. Lu, Y. L. Chueh and B. Xiang, *J. Power Sources*, 2020, **477**, 229022.
12 Z. Pu, T. Liu, I. S. Amiinu, R. Cheng, P. Wang, C. Zhang, P. Ji, W. Hu, J. Liu and S. Mu, *Adv. Funct. Mater.*, 2020, **30**, 1–23.
13 J. K. Das, A. K. Samantara, S. Satyarthy, C. S. Rout and J. N. Behera, *RSC Adv.*, 2020, **10**, 4650–4656.
14 Q. Zong, C. Liu, H. Yang, Q. Zhang and G. Cao, *Nano Today*, 2021, **38**, 101201.
15 X. Shi, L. Sun, X. Li, L. Wu, J. Qian, J. Wang, Y. Lin, S. Su, C. Sun, Y. Zhang and Y. Zhang, *J. Colloid Interface Sci.*, 2022, **606**, 135–147.
16 R. Dubey and V. Guruviah, *Ionics*, 2019, **25**, 1419–1445.
17 J. Gou, Y. Du, S. Xie, Y. Liu and X. Kong, *Int. J. Hydrogen Energy*, 2019, **44**, 27214–27223.
18 Z. Wang, H. Wang, S. Ji, X. Wang, P. Zhou, S. Huo, V. Linkov and R. Wang, *Mater. Des.*, 2020, **193**, 108807.
19 X. Zhang, L. Zhang, G. Xu, A. Zhao, S. Zhang and T. Zhao, *J. Colloid Interface Sci.*, 2020, **561**, 23–31.
20 Z. Huang, X. Li, X. Xiang, T. Gao, Y. Zhang and D. Xiao, *J. Mater. Chem. A*, 2018, **6**, 23746–23756.
21 P. Li, M. Zhang, H. Yin, J. Yao, X. Liu and S. Chen, *Appl. Surf. Sci.*, 2021, **536**, 147751.
22 X. He, Y. Niu, H. Sun, X. Chen, Z. Wang, J. Jiang and C. Wang, *J. Alloys Compd.*, 2023, **930**, 167316.
23 Z. Zeng, Y. Liu, W. Zhang, H. Chevva and J. Wei, *J. Power Sources*, 2017, **358**, 22–28.
24 X. Yu, J. Yu, W. Zhang, Q. Lv, W. Ren, L. Hou, Y. Fautrelle, X. Lu and X. Li, *Chem. Eng. J.*, 2022, **446**, 137107.
25 X. Yu, W. Zhang, L. Liu, Y. Fautrelle, X. Lu and X. Li, *ACS Appl. Mater. Interfaces*, 2020, **12**, 33690–33701.
26 M. Singh, A. Sahoo, K. L. Yadav and Y. Sharma, *Appl. Surf. Sci.*, 2021, **568**, 150966.
27 X. Han, J. Li, J. Lu, S. Luo, J. Wan, B. Li, C. Hu and X. Cheng, *Nano Energy*, 2021, **86**, 106079.
28 H. Li, S. Lin, H. Li, Z. Wu, Q. Chen, L. Zhu, C. Li, X. Zhu and Y. Sun, *Small Methods*, 2022, **6**, 1–12.
29 L. Li, L. Shao, Y. Sun, D. Yuan, Z. Jiao, Y. Sun, X. Tian, T. Fei, Y. Peng, L. Zhang and X. Xu, *J. Alloys Compd.*, 2024, **983**, 173883.
30 E. Baasanjav, T. G. Senthamaraikannan, P. Bandyopadhyay, D. H. Lim and S. M. Jeong, *Chem. Eng. J.*, 2023, **466**, 143064.
31 V. Sharma, S. Biswas and A. Chandra, *Adv. Energy Mater.*, 2018, **8**, 1–12.
32 H. Wei, H. Gu, J. Guo, D. Cui, X. Yan, J. Liu, D. Cao, X. Wang, S. Wei and Z. Guo, *Adv. Compos. Hybrid Mater.*, 2018, **1**, 127–134.
33 S. Raj K A and C. S. Rout, *J. Mater. Chem. A*, 2023, **11**, 5495–5519.
34 L. Zhang, Z. Zeng, D. W. Wang, Y. Zuo, J. Chen and X. Yan, *Cell Rep. Phys. Sci.*, 2021, **2**, 100455.
35 S. T. Aziz, S. Kumar, S. Riyajuddin, K. Ghosh, G. D. Nessim and D. P. Dubal, *J. Phys. Chem. Lett.*, 2021, **12**, 5138–5149.
36 S. Mondal, U. Rana and S. Malik, *J. Phys. Chem. C*, 2017, **121**, 7573–7583.
37 M. Yi, B. Lu, X. Zhang, Y. Tan, Z. Zhu, Z. Pan and J. Zhang, *Appl. Catal., B*, 2021, **283**, 119635.
38 A. Viswanathan and A. N. Shetty, *Electrochim. Acta*, 2019, **309**, 187–196.

39 W. Pholauyphon, P. Charoen-amornkitt, T. Suzuki and S. Tsushima, *J. Energy Storage*, 2024, **98**, 112833.
40 S. Pal, S. Majumder, S. Dutta, S. Banerjee, B. Satpati and S. De, *J. Phys. D: Appl. Phys.*, 2018, **51**, 375501.
41 S. K. Sundriyal and Y. Sharma, *ACS Appl. Energy Mater.*, 2020, **3**, 6360–6373.
42 N. Kumar, M. Singh, A. Kumar, T. Y. Tseng and Y. Sharma, *ACS Appl. Energy Mater.*, 2020, **3**, 2450–2464.
43 N. Sinan and E. Unur, *Mater. Chem. Phys.*, 2016, **183**, 571–579.
44 G. Kresse and J. Furthmüller, *Phys. Rev. B: Condens. Matter Mater. Phys.*, 1996, **54**, 11169–11186.
45 G. Kresse and J. Furthmüller, *Comput. Mater. Sci.*, 1996, **6**, 15–50.
46 H. J. Monkhorst and J. D. Pack, *Phys. Rev. B*, 1976, **13**, 5188–5192.
47 D. L. John, L. C. Castro and D. L. Pulfrey, *J. Appl. Phys.*, 2004, **96**, 5180–5184.
48 D. Chakrabartty, M. Sahoo, A. Kumar, S. Jamaluddin, B. Giri, H. Chhabra, K. Pradhan and A. K. Nayak, *ACS Nano*, 2025, **19**, 3614–3623.
49 M. R. Sahoo, S. K. Nayak and K. Pradhan, *J. Phys. Chem. C*, 2022, **126**, 4638–4646.
50 A. Shah, S. Senapati, H. C. A. Murthy, L. R. Singh and M. Mahato, *ACS Omega*, 2023, **8**, 33380–33391.
51 M. Wang, H. Wang, X. Zhang, D. Chen, N. Wang, M. Qin and J. Yang, *Appl. Surf. Sci.*, 2023, **636**, 157820.
52 B. Üstün, H. Aydın, S. Naci Koç and Ü. Kurtan, *Fuel*, 2023, **341**, 127735.
53 A. M. Palve, O. V. Vani, R. Srivastava, W. Lin and R. K. Gupta, *Heliyon*, 2025, **11**, e42414.
54 M. Singh, A. Sahoo, K. L. Yadav and Y. Sharma, *ACS Appl. Mater. Interfaces*, 2020, **12**(44), 49530–49540.
55 J. Halder, S. Biswas, A. Chowdhury, D. Mandal, S. Kansal, S. Priya, P. De, A. K. Srivastava and A. Chandra, *J. Phys. Chem. C*, 2023, **127**, 14623–14635.